Journal of Thermal Analysis and Calorimetry (2020) 142:1315–1327
https://doi.org/10.1007/s10973-019-09169-6

Exploration of the thermal decomposition of zinc oxalate by experimental and computational methods

K. Sabira[1] · **K. Muraleedharan**[1]

Received: 31 May 2019 / Accepted: 6 December 2019 / Published online: 7 February 2020

Abstract

Zinc oxalate dihydrate has been synthesized by precipitation method and characterized by FT-IR, XRD and SEM-EDAX. The kinetics of dehydration and decomposition were studied by non-isothermal DSC technique in the N_2 atmosphere at different heating rates: 4, 6, 8 and 10 K min^{-1}. The product of thermal decomposition, ZnO has been characterized by UV, TEM, SEM-EDAX and XRD and found that the particles are in nanometer range. The activation energy for thermal dehydration and decomposition was calculated by various isoconversional methods. Furthermore, structure and reactivity of zinc oxalate have also been investigated using B3LYP/631+g (d, p) level of theory with the help of Gaussian 09W software. The theoretical investigation indicates that most probably the compound decomposes to ZnO along with the evolution of CO_2 and CO.

Keywords Zinc oxalate dihydrate · Thermal decomposition · Dehydration · Isoconversional methods

Introduction

Thanks to the advancement of nanotechnology and nanophase engineering which expands the manipulation of mechanical, catalytic, electric, magnetic, optical and electronic properties of materials, the necessity of encapsulation during the synthesis of nanomaterials in solution (chemical route) and the difficulty of obtaining pure nanoparticles make the scientists think of alternate routes. Thermal decomposition of metal oxalates has been investigated by many researchers for more than a century [1–12]. Metal oxalates act as good precursors for the synthesis of metal oxide nanoparticles since their thermal decomposition affords homogenous oxide nanoparticles with low cost and can be easily transformed to metal oxides at low temperatures. The resultant metal oxide nanoparticles are receiving growing attention because of their important optical, mechanical, electrical, magnetic and catalytic behavior [13]. The potential applications of nanosized transition metals and their oxides make their study as a very hot topic in material science. The possibility of obtaining nanocrystalline transition metal oxides by the thermal decomposition of the parent oxalates and the kinetics of their thermal decomposition are not investigated in depth. The thermal data obtained from TG or DSC at different heating rates can be analyzed by model fitting or model-free isoconversional methods. The knowledge of kinetic parameters such as reaction model, Arrhenius pre-exponential factor and activation energy of thermal reaction of solids is one of the keys to determine the reaction mechanism in solid phases.

ZnO is an n-type semiconductor of band gap 3.37 eV and exciton binding energy of 60 M eV [14]. Owing to its high quantum efficiency, several researchers confirmed that it is a better photocatalyst for the degradation of organic pollutants over TiO_2 [15–17]. Few papers are concerned with the thermal decomposition of ZnC_2O_4 [18–22]. Decomposition of zinc oxalate in an inert atmosphere is a simple, one-stage reaction, leading to the formation of solid ZnO and CO and CO_2 as gaseous products. Decomposition of ZnC_2O_4 in a nitrogen atmosphere is a first-order reaction with an activation energy of 435 kJ mol^{-1} [19]. Kornienko studied the kinetics of isothermal decomposition of ZnC_2O_4 in an atmosphere of CO, CO_2 and H_2O and described the reaction by Avrami–Erofeev equation with $n=2$ and an activation energy of 183 kJ mol^{-1} [23]. Małecka [23] studied thermal decomposition of ZnC_2O_4 in helium atmosphere in isothermal and non-isothermal conditions and found decomposition is a single-stage reaction

Electronic supplementary material The online version of this article (https://doi.org/10.1007/s10973-019-09169-6) contains supplementary material, which is available to authorized users.

✉ K. Muraleedharan
kmuralika@gmail.com

[1] Department of Chemistry, University of Calicut, Malappuram 673635, India

with ZnO as a final product and described by Avrami–Erofeev equation with $n \approx 2$ for both non-isothermal and isothermal measurements. The activation energy of ZnC_2O_4 decomposition is 181.4–186.5 and 190.8 kJ mol^{-1} for non-isothermal and isothermal conditions, respectively. Hu [24] investigated the decomposition of ZnC_2O_4, and the activation energy obtained from the DTA data by the non-isothermal method is 119.7 kJ mol^{-1} and $G(\alpha) = -\ln(1-\alpha)^{(1/2)}$. Since there are significant discrepancies between kinetic data of decomposition of ZnC_2O_4, confusion still remains in the mechanism of decomposition and kinetics for each possible step in the mechanism. This study focused on the elucidation of the kinetics and mechanism of thermal dehydration of $ZnC_2O_4{\cdot}2H_2O$ and the thermal decomposition of ZnC_2O_4 by non-isothermal DSC technique in flowing N_2 atmosphere. The absence of steady portrayal and clarification of the origin and thermal decomposition way of oxalates from the experimental outcomes made us think for the theoretical clarification of the same. The experimental discoveries can be rationalized through density functional theory (DFT)-based computational investigation [25]. It appears to be sensible to expect that the theoretical investigation of the fundamental features of electron density (topological analysis) and chemical bond (bond order, bond length, etc.) should in principle lead to the forecast of the decomposition pathways for metal oxalates [26]. Kolezyn'ıski et al. [27–32] have recently done the theoretical examination of electronic structure and bonding properties of many transition metal oxalates (including zinc oxalate) which is extremely encouraging and not just gave us extra understanding into the thermal decomposition process in those oxalates yet, in addition, depicted it as a progression of consecutive bond breaking steps proceeding in the theoretically anticipated order. Their whole investigation depended on the topological examination of electron density (Bader's quantum theory of atoms in molecule formalism) [26] got from first-principles FP-LAPW calculations and structural and bonding properties—bond valence, bond strength and stresses—related to a deviation of given structure from perfect one (Brown's bond valence method). The target of the present work is to examine the dehydration of zinc oxalate dihydrate and the thermal decomposition behavior of anhydrous zinc oxalate by experimental techniques by non-isothermal DSC technique in flowing N_2 atmosphere and furthermore by theoretical examination of the electronic structure and bonding properties in view of the DFT strategy utilizing Gaussian 09W simulation package.

Experimental

Materials

The reagents used in this study are of analytical grade and employed without any further purification. The chemicals used in the study are $ZnCl_2{\cdot}4H_2O$ (HiMedia, India) and $H_2C_2O_4$ (Merck, India).

Methods

Preparation of zinc oxalate dihydrate

An equimolar ratio of $ZnCl_2{\cdot}4H_2O$ and $H_2C_2O_4$ was separately mixed in distilled water to form a homogenous solution. These were mixed thoroughly under vigorous stirring condition up to the formation of white precipitate of $ZnC_2O_4{\cdot}2H_2O$

$$ZnCl_2{\cdot}4H_2O + H_2C_2O_4 \rightarrow ZnC_2O_4{\cdot}2H_2O + 2HCl + 2H_2O.$$

The precipitate was washed several times with distilled water and dried in an air oven. The sample prepared was sieved through the mesh, and the particle size was fixed in the range of 95–105 µm. The prepared zinc oxalate dihydrate samples then were calcined at 473, 683 and 773 K by placing it in a muffle furnace which has an air atmosphere. The product of thermal decomposition of zinc oxalate is zinc oxide. Similarly, when zinc oxalate is calcined, the product is zinc oxide, not zinc metal. If the product of decomposition/calcination is zinc metal, then there is a possibility of zinc oxide formation when it is placed in air atmosphere by the reaction with oxygen present in air. In this case, such problem will not rise.

Preparation of pelletized samples

The samples were well grounded, and the powdered samples were pressed using the hydraulic pellet press (KP, SR. No. 1718) under a pressure of 50 kg cm^{-2}. Zinc oxalate dihydrate and thermally heated samples (473, 683 and 773 K) were also pelletized using hydraulic press under the same pressure.

Characterization of the sample

Fourier transform infrared (FT-IR) spectra of the samples was recorded by transmittance method using a spectrometer (model Jasco FT-IR-4100) after diluting the samples with KBr powder. The optical band gap (E_g) of the decomposed product was calculated from UV–Visible reflectance which was measured using UV–Visible diffuse reflectance spectrum (model Jasco V-550 spectrophotometer). The powder X-ray diffraction (XRD) patterns of the samples were recorded using a diffractometer (Miniflex 600, model RigakuD/Max) with Cu-Kα ($\lambda = 1.5418$ Å) radiation (40 kV, 15 mA) with a scan rate of 2θ min^{-1} in the region of 20°–90°. The scanning electron microscopic (SEM) analyses of all the samples studies were performed with SEM-EDAX combination using

Carl Zeiss Gemini SEM 300. The transmission electron microscopic (TEM) analysis of the particles was carried out by using a JEOL model JEM 2100 field emission transmission electron microscope operated at 200 kV with a 0.18 nm resolution.

Measurement of thermal behavior

TG measurements were taken on a PerkinElmer Pyris thermal analyzer STA8000 at two heating rates 6 and 8 K min^{-1}. The operational characteristics of the thermal analysis system are as follows: atmosphere: flowing N_2, at a flow rate of 20 mL min^{-1}, sample mass: ~10 mg; and sample pan: aluminum. Duplicate runs were made under similar conditions and found that the data overlap with each other, indicating satisfactory reproducibility. The differential scanning calorimetric (DSC) measurements of the samples were taken in the temperature range 303–773 K at four different heating rates, viz. 4, 6, 8 and 10 K min^{-1}, on a Mettler Toledo DSC822e. The operational characteristics of the DSC system are as follows: atmosphere: flowing N_2 at a flow rate of 50 mL min^{-1}; sample mass ~5.1 mg; and sample holder: aluminum.

Computational methodology

The theoretical analysis of the molecule has been done based on the DFT method. The structure is optimized using DFT with 6-31+g (d, p) as basis set. The level of theory adopted was B3LYP, which consists of Becke's exchange functional [33] in conjunction with the Lee–Yang–Parr correlation functional [34]. All the computational works were done through Gaussian 09W software package. Global reactivity descriptors like ionization potential, electron affinity, electronegativity, electrophilicity, softness, hardness, etc., are calculated in order to analyze the extent of reactivity of the molecule.

Global reactivity descriptors

Global reactivity descriptors can be calculated by energy vertical and orbital vertical methods. In the latter, global reactivity descriptors can be written as follows which make use of approximation suggested by Koopman's theorem.

$$\text{Ionisation } p\text{otential (IP)} \approx -E_{\text{HOMO}} \tag{1}$$

$$\text{Electron } a\text{ffinity(EA)} \approx -E_{\text{LUMO}} \tag{2}$$

where E_{HOMO} is the energy of HOMO and E_{LUMO} is the energy of LUMO

$$\text{Hardness } (\eta) \approx (\text{IP}-\text{EA})/2 \tag{3}$$

$$\text{Electronegativity } (\chi) \approx (\text{IP}+\text{EA})/2 \tag{4}$$

$$\text{Softness } (S) \approx 1/2\eta \tag{5}$$

$$\text{Chemical potential } (\mu) \approx -\chi \tag{6}$$

$$\text{Electrophilicity index } (\omega) \approx \mu^2/2\eta \tag{7}$$

Results and discussions

Sample characterization

Figure 1a represents the FT-IR spectra of $ZnC_2O_4{\cdot}2H_2O$ and ZnC_2O_4 calcined at 473, 683 and 773 K, and Fig. 1b indicates the IR spectra of $ZnC_2O_4{\cdot}2H_2O$, ZnC_2O_4 and ZnO using 6-31+g (d, p) as basis set. The FT-IR spectrum obtained for zinc oxalate dihydrate is compared with that of a theoretical one. Both of them have almost similar vibrational frequencies. The slight shift in values between theoretical and experimental data is due to the effect of solvent and the IR measuring conditions. The strong broadband centered at about 3396 cm^{-1} is assigned to stretching modes of hydrated water, υ(O–H); this band arises due to the presence

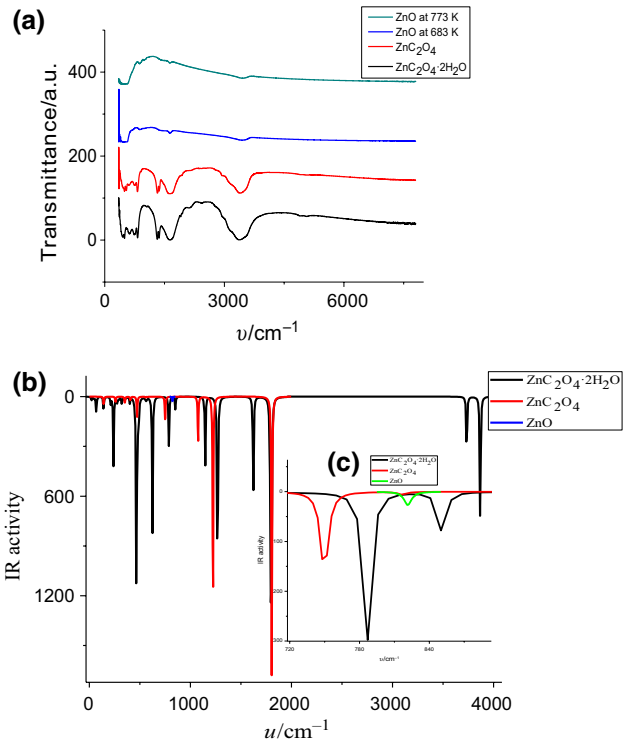

Fig. 1 FT-IR spectra of $ZnC_2O_4{\cdot}2H_2O$ and ZnC_2O_4 calcined at 473, 683 and 773 K (**a**), IR spectra of $ZnC_2O_4{\cdot}2H_2O$, ZnC_2O_4 and ZnO using 6-31+g (d, p) as basis set (**b**) and inset graph (**c**) shows the enlarged portion of graph (**b**)

of water in the sample. Computationally obtained value for O–H stretching is around 3800 cm^{-1}. The strong band at 1621 cm^{-1} is characteristic of C=O antisymmetric stretching modes υ_{as}(C=O). The theoretical value obtained for the same is 1788 cm^{-1}. The small peaks at 1356 and 1318 cm^{-1} is due to the O–C–O stretching modes, and its corresponding theoretical values are 1268 and 1145 cm^{-1}; the small bands at 827 and 461 cm^{-1} are due to the O–C=O bending modes υ(O–C=O) and Zn–O stretching modes υ (Zn–O). From computational studies, Zn–O stretching frequency for zinc oxalate is 471.5 cm^{-1}. Theoretical studies of ZnO using 6-31+g (d, p) as basis set show Zn–O stretching frequency as 821 cm^{-1} which clearly indicated that the vibration of the Zn–O bond is highly affected by the oxalate ligands. FT-IR spectra of ZnO calcined at 683 and 773 K show only the stretching mode of Zn–O at 461 cm^{-1}, indicating that ZnO only is the final product [24]. The FT-IR spectra obtained for $ZnC_2O_4{\cdot}2H_2O$ and ZnO were also compared with the FT-IR spectra reported by Hu et al. [24] and found that the bands obtained were perfectly matched with the reported values. Hu et al. [24] got the bands at 3394, 1634, a double band at 1364 and 1319, a small band at 822 and one at 496 cm^{-1} and they ascribed these bands to stretching modes of hydrated water, C=O antisymmetric stretching modes, O–C–O stretching modes, O–C=O bending modes and Zn–O stretching modes, respectively.

Powder XRD patterns of the sample and thermally heated samples at 473, 683 and 773 K are shown in Fig. 2 The average crystallite size was calculated using the Debye–Scherrer equation [35].

$$D = K\lambda/\beta \mathrm{Cos}\theta \tag{8}$$

where β is the full width at half maximum intensity of the peak (in Rad), K is the crystallite shape factor, a good approximation is 0.9, λ is the wavelength of the incident X-ray ($\lambda = 0.1540$ nm for Cu-Kα), D is the crystallite size and θ is the Bragg angle in degree. The XRD patterns obtained for the sample calcined at 683 and 773 K show the peaks corresponding to ZnO only. The XRD peaks obtained is well matched with the previously reported one which was synthesized through oxalate precipitation route [24]. XRD peaks can be indexed on zinc oxide of hexagonal wurtzite phase (JCPDS card no. 36–1451, a, $b = 3.256$ nm, $c = 5.22$ nm). The peaks at 2θ values 31.59, 34.18, 36.12, 47.41, 56.43, 62.56, 66.43, 67.89 and 68.86 represent (100), (022), (101), (102), (110), (103), (200), (112) and (201) planes of wurtzite ZnO. As the calcination temperature increases from 683 to 773 K, ZnO does not decompose, but the crystallinity of ZnO increases. This is evident from the XRD patterns of ZnO calcined at 683 and 773 K. The obtained average crystallite size using Debye–Scherrer equation was 22.36 and 44.00 nm for the synthesized ZnO nanoparticles at 683 and 773 K, respectively.

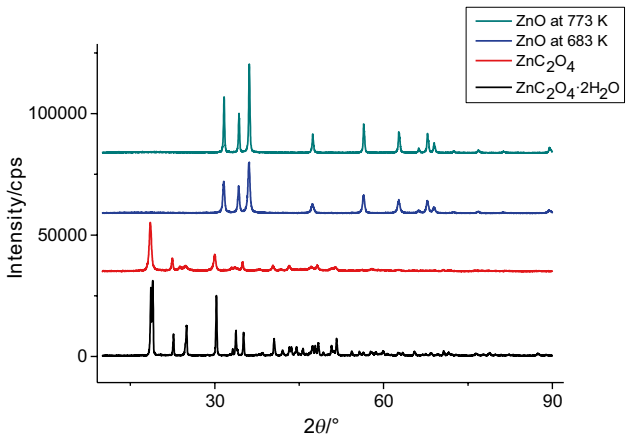

Fig. 2 Powder XRD patterns of $ZnC_2O_4{\cdot}2H_2O$ and ZnC_2O_4 calcined at 473, 683 and 773 K

TEM images of the ZnO calcined at 773 K are shown in Figs. 3a, b and its SAED pattern in (c). Figure 3d represents the lattice fringes of the synthesized nanoparticles. TEM images indicate that ZnO nanospheres are formed and their size distribution is not homogeneous. The smallest particle has an average size of 36 nm. TEM images and SAED pattern revealed the high crystallinity of the sample. HR-TEM images reveal that chain-like structure is formed by the ZnO nanoparticles. The clear lattice fringes also demonstrated that the nanoparticles are highly crystalline and obtained a lattice spacing of 0.22 nm.

Figure 4a–d shows the SEM images of the sample and thermally heated sample at 473, 683 and 773 K. The morphology of the precursor, $ZnC_2O_4{\cdot}2H_2O$ is timber-like. SEM images of the formed ZnO nanoparticles at 683 K show small rodlike morphology; further heating the sample alters the morphology of ZnO nanoparticles and forms spherical ZnO nanoparticles at 773 K. The SEM images obtained for $ZnC_2O_4{\cdot}2H_2O$ and ZnO calcined at 773 K were compared with the previously reported ones [36, 37]; it is found that the particle size ranges of ZnO nanoparticles and their morphology were well agreed with the literature. Figure 4e represents SEM image of ZnO nanoparticles formed by calcining $ZnC_2O_4{\cdot}2H_2O$ at 773 K and shows that at some locations the formed spherical nanoparticles makes chain-like structures that accord well with SEM images.

A combination of SEM–EDS (energy-dispersive X-ray spectroscopy EDS, EDAX, EDXS or XEDS) is used for the elemental analysis of the sample and thermally heated samples at 473, 683 and 773 K. Mass percentages of different elements are given in Table 1. The result is consistent with their molecular formula.

The optical band gap (E_g) of the decomposed product was calculated from UV–Vis reflectance which was measured

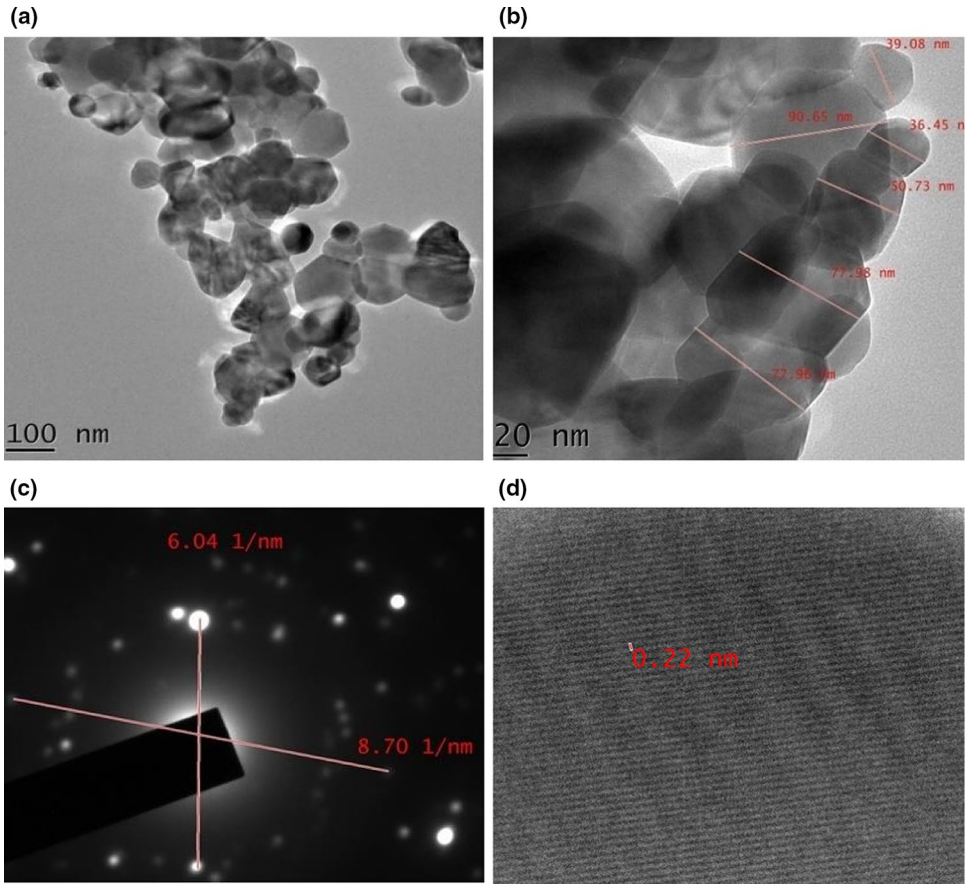

Fig. 3 TEM images of ZnO nanospheres calcined at 773 K (**a**) and (**b**), SAED pattern (**c**) and lattice fringes of the synthesized nanoparticles (**d**)

using UV–Vis diffuse reflectance spectrum. The optical band gap is determined by using the Tauc equation

$$(\alpha h\upsilon)^{n} = B\left(h\upsilon - E_{g}\right) \tag{9}$$

where $h\upsilon$ is the photon energy, α is the absorption coefficient, B is a constant relative to the material and n is either 2 for direct transition or 1/2 for an indirect transition. The $(\alpha h\upsilon)^2$ versus $h\upsilon$ curve (Tauc plot) of ZnO calcined at 773 K is shown in Fig. 5, and the band gap obtained was 3 eV. The obtained band gap value was compared with the band gap value reported by Nelsa et al. [38] who synthesized ZnO through oxalate precipitation route, and found that the values are well agreed with each other.

Characterization of thermal decomposition behavior

Figure 6 shows the result of the thermogravimetric analysis of $ZnC_2O_4{\cdot}2H_2O$ at two heating rates 6 and 8 K min^{-1}. The figure shows two different mass loss stages corresponding to dehydration and decomposition. There is a small increase in the temperature of dehydration and decomposition with the increase in heating rate. The first mass loss of 18.60% around 402.36–449.00 K is consistent with the elimination of 1.96 mol of water molecules. The second mass loss of 37.52% (theoretical mass loss 38.03%) around the temperature of 626.92–694.92 K indicates the decomposition of ZnC_2O_4. The total mass loss is 56.12%, which is in good agreement with the calculated value of 57.10% that can be calculated if it is assumed that the $ZnC_2O_4{\cdot}2H_2O$ is completely transformed into ZnO [24]. The obtained TG was juxtaposed with the TG reported by Barbara et al. [23] and Hu et al. [24], and it was found that the results agreed with these ones. Barbara et al. [23] reported that the elimination of 1.88 mol of water molecule in the dehydration stage and decomposition stage starts above 600 K. Hu et al. [24] found that dehydration stage occurred in the temperature range 363–444 K with the removal of 2 mol of water and the decomposition stage took place in the temperature range 573–673 K with a mass loss of 37.2%.

Figure 7 shows the DSC curves of $ZnC_2O_4{\cdot}2H_2O$ at different heating rates: 4, 6, 8 and 10 K min^{-1}. DSC curves show two endothermic peaks corresponding to dehydration (around 423.7–441.9 K) of two molecules of water from $ZnC_2O_4{\cdot}2H_2O$ and the decomposition (around 656.6–676.7 K) of ZnC_2O_4. The two stages were well separated from each other, and there is a slight shift in the temperatures of the dehydration and decomposition

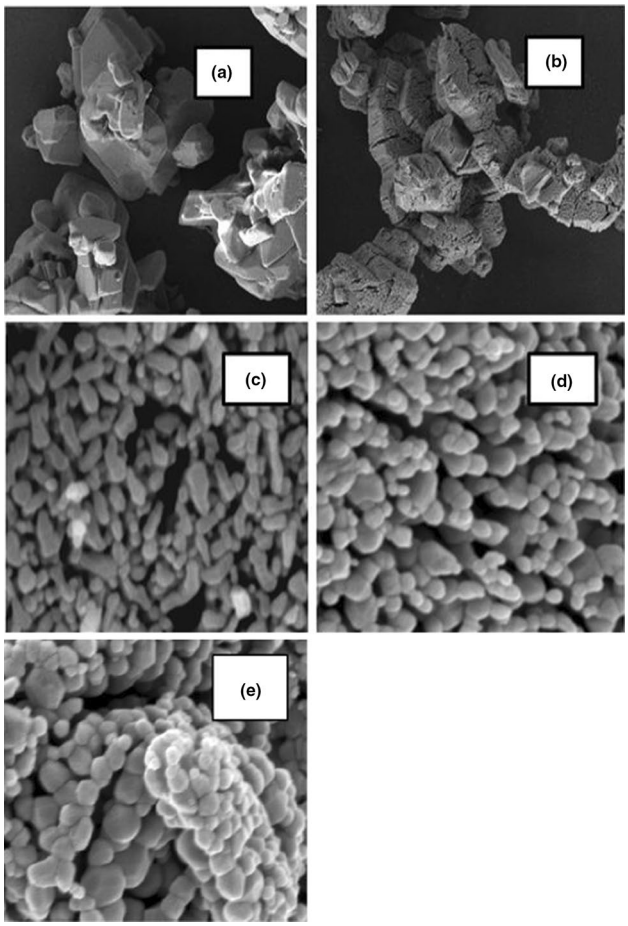

Fig. 4 SEM images of $ZnC_2O_4{\cdot}2H_2O$ (**a**), ZnC_2O_4 calcined at 473 (**b**), 683 (**c**) and 773 K (**d**), (**e**)

reaction with an increase in heating rates as observed in TG. The peaks for dehydration and decomposition reactions become sharper with an increase in heating rate which indicated that reactions are kinetically controlled.

Kinetic behavior

The kinetic parameters of solid-state decomposition reaction proceeding non-isothermal conditions can be studied using the differential form of the kinetic equation;

$$d\alpha/dt = k(T)f(\alpha) \tag{10}$$

where $f(\alpha)$ is a function of α depending on reaction model and

$$k(T) = Ae^{-E_a/RT} \tag{11}$$

where E_a is the activation energy and A is the pre-exponential factor. Arrhenius parameters can be determined only if $k(T)$ and $f(\alpha)$ are separated. Out of model fitting which is based on the single heating curve and model-free method of kinetic analysis, model-free isoconversional methods at multiple heating curves are the most dependable for calculating activation energy of thermal decomposition reaction in non-isothermal conditions [39, 40]. Isoconversional methods assume that the reaction rate at a fixed α depends only on temperature and reaction model is independent of heating rates. Reaction rate alters with the heating rate. The reaction rate is fast at the higher heating rate. The variation in the rate of reaction at different heating rates can be used to determine the activation energy of the reaction. Activation energy is constant throughout the conversion for a single-stage reaction, while it varies for complex reactions. The mechanism of the reaction can be explained by studying the variation of activation energy with α. Starink [41] compared the accuracy of different isoconversional methods in the determination of activation energy from linear heating rate experiments.

Combining Eq. (11) in (10),

$$d\alpha/dt = Ae^{-E_a/RT}f(\alpha) \tag{12}$$

At non-isothermal conditions, the temperature is increasing with time at the constant heating rate. Integration of Eq. (12) involves solving the temperature integral, $I(E, T)$

$$g(\alpha) = A/\beta \int_0^{Tx} e^{-E_a/RT}dt = A/\beta I(E,T) \tag{13}$$

This equation has an ineffectual analytical solution. Some approximations or numerical integration is used to solve the equation. All of the approximations lead to a direct isoconversional method in the form:

$$\ln\left(\beta/T^K\right) = C - E_a/RT \tag{14}$$

For a selected degree of conversion function, α, a corresponding $T_{\alpha i}$ and heating rate β are used to plot ln (β/T^K)

Table 1 Mass percentages of different elements from SEM–EDS

Sample	Elements	Mass%	Atomic%
$ZnC_2O_4{\cdot}2H_2O$	C	14.89	28.90
	O	37.01	53.94
	Zn	48.10	17.16
ZnC_2O_4	C	16.60	32.93
	O	32.61	48.56
	Zn	50.79	18.51
ZnO at 683 K	O	14.57	41.07
	Zn	85.43	58.93
ZnO at 773 K	O	15.99	43.74
	Zn	84.01	56.26

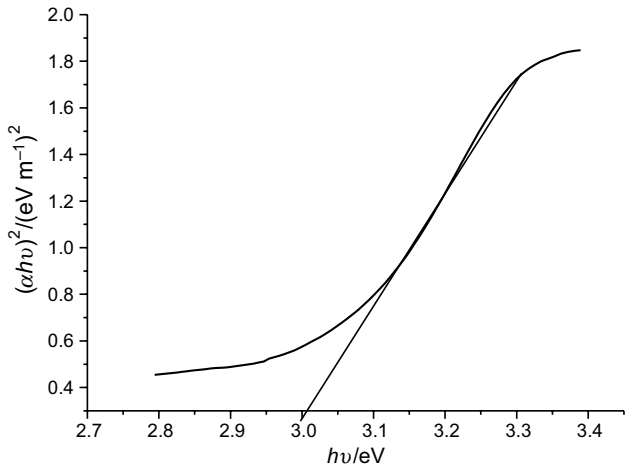

Fig. 5 Tauc plot of ZnO calcined at 773 K

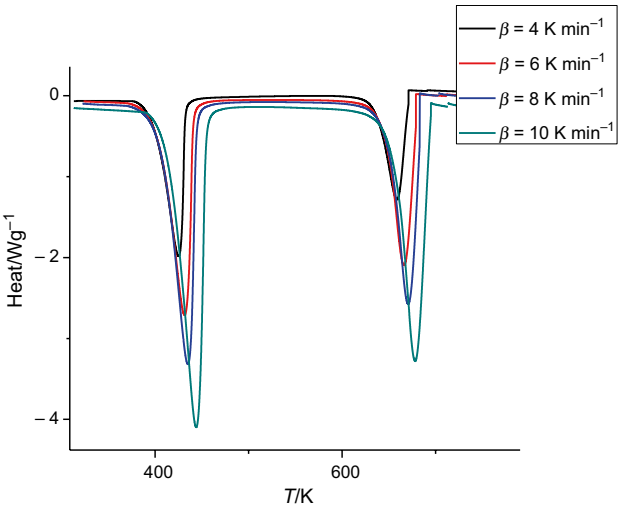

Fig. 7 DSC curves of $ZnC_2O_4{\cdot}2H_2O$ at different heating rates: 4, 6, 8 and 10 K min^{-1}

against $1/T_{\alpha i}$, where K is a constant. The activation energy is then determined from the regression slope [42].

Isoconversional methods for the calculation of E_a

Flynn–Wall–Ozawa (FWO) method [43, 44]

$$\ln \beta = \ln (AE/g(\alpha)R) - 5.331 - 1.052E_{\alpha}/RT_{\alpha i} \quad (15)$$

where α is the conversion function. From the slope of the graph $\ln\beta$ against $1/T_{\alpha i}$, E_a can be calculated.

Kissinger–Akahira–Sunose (KAS) method [45]

KAS is also an integer isoconversional method similar to FWO.

$$\ln \beta/T^2 = \ln \left(AR/E_a g(\alpha)\right) - E_a/RT \quad (16)$$

E_a can be obtained from the slope of the straight-line graph $\ln\beta/T^2$ against $1/T$.

Tang method [46]

$$\ln \left(\beta/T^{1.894661}\right) = \ln \left(AE_a/Rg(\alpha)\right) + 3.635041 - 1.894661 \ln E_a - 1.00145033E_a/RT \quad (17)$$

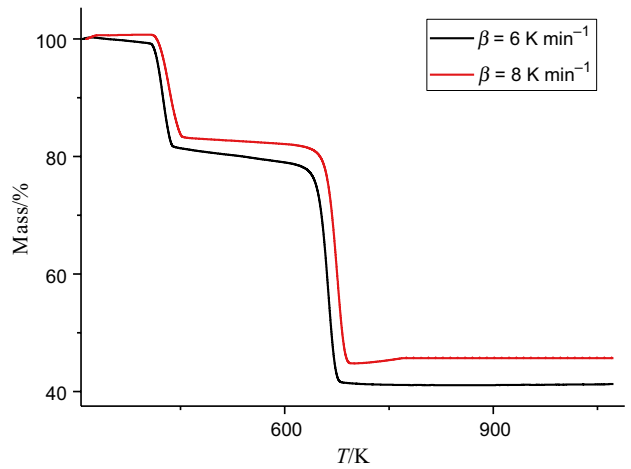

Fig. 6 TG curve of $ZnC_2O_4{\cdot}2H_2O$ at the heating rates 6 and 8 K min^{-1}

E_a can be obtained from the slope of the straight-line graph $\ln(\beta/T^{1.894661})$ against $1/T$.

Starink method [41]

$$\ln \beta/T^{1.95} = C^{1.95}(\alpha) - E_a/RT \quad (18)$$

$$\ln \beta/T^{1.92} = C^{1.92}(\alpha) - 1.0008E_a/RT \quad (19)$$

Bosewell method

$$\ln \beta/T = C(\alpha) - E_a/RT_{\alpha i} \quad (20)$$

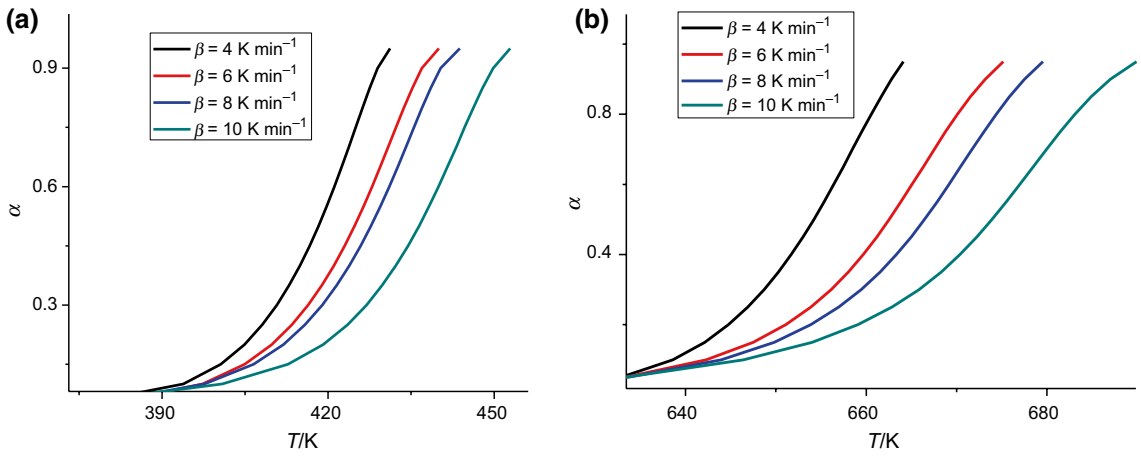

Fig. 8 α—T plots for dehydration of $ZnC_2O_4{\cdot}2H_2O$ (**a**) and decomposition of ZnC_2O_4 (**b**) at different heating rates: 4, 6, 8 and 10 K min^{-1}

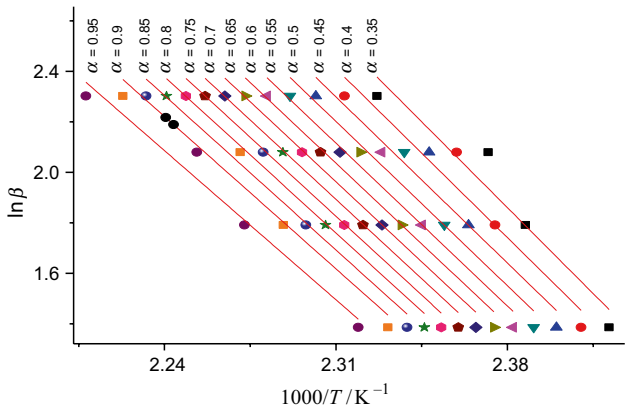

Fig. 9 Typical linear least squares plot for the dehydration stage of $ZnC_2O_4{\cdot}2H_2O$ for the isoconversional method FWO

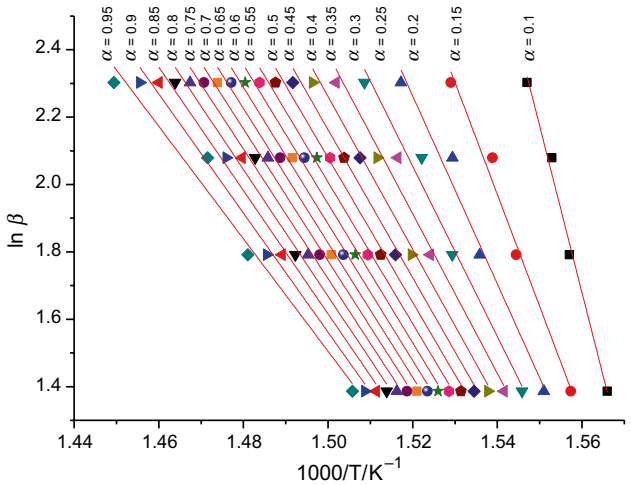

Fig. 10 Typical linear least squares plot for the decomposition stage for the isoconversional method FWO

Friedman method

It is mathematically exact since it does not use any approximation. The method is advisable if dα/dt is measured unambiguously at a fixed value of α. DSC experiments are sentient of the baseline stability, so dα/dt is strenuous to obtain for several experiments. Based on Eq. (12), ln (dα/dt) versus T^{-1} at different α for the series of kinetic data recorded under linear non-isothermal condition were plotted to determine the values of E_a at different α and to study its variation with α.

Thermal decomposition of $ZnC_2O_4{\cdot}2H_2O$ proceeds through dehydration of two molecules of water. DFT WIEN2k FP-LAPW ab initio package calculations for zinc oxalate by Kolezynski and Malecki suggest that the thermal decomposition of ZnC_2O_4 starts with the breakage of Zn–O bond forming a partially anchored oxalate ion. The C–C bond then breaks to produce CO_2, and the CO_2^{2-} then decomposes to ZnO and CO. This is evident from their topological analysis that in all cases, the C_1–O_1 bond is strongest, then much weaker are C_1–O_2^i and C_1–C_2 bonds (the latter one is little stronger) and the weakest are Zn–O bonds [28].

The conversion function α in the range 0.05–0.95 with an interval of 0.05 and their corresponding temperatures are calculated from the experimental heat change data procured from DSC for the dehydration and decomposition reactions. These α–T data were subjected to linear least squares analysis using various model-free isoconversional methods like FWO, KAS, Tang, Starink$^{1.95}$, Starink$^{1.92}$, Bosewell and Friedman. The α–T plots for dehydration and decomposition at different heating rates, 4, 6, 8 and 10 K min^{-1}, are shown in Fig. 8. The activation energy values were evaluated from the slope of the linear least squares plots. Typical linear least squares plot for the two reaction stages, dehydration and thermal decomposition, for the isoconversional method FWO is shown in Figs. 9 and 10. Linear least squares plots

Table 2 Values of activation energy (E_a) in kJ mol^{-1} obtained through linear least squares analysis for the isoconversional methods of FWO, KAS, Tang, Starink$^{1.95}$, Starink$^{1.92}$, Bosewell and Friedman for the dehydration reaction

α	E_a/kJ mol^{-1}						
	FWO	KAS	Tang	Starink$^{1.95}$	Starink$^{1.92}$	Bosewell	Friedman
0.10	165.40	167.39	167.49	167.56	167.52	170.69	
0.15	98.62	96.99	97.20	97.16	97.18	100.37	
0.20	86.44	84.08	84.32	84.25	84.29	87.51	
0.25	81.37	78.69	78.94	78.86	78.90	82.15	
0.30	78.70	75.82	76.08	76.00	76.04	79.31	60.41
0.35	76.80	73.79	74.05	73.97	74.01	77.29	60.92
0.40	75.54	72.43	72.69	72.60	72.65	75.95	60.56
0.45	74.29	71.07	71.34	71.25	71.30	74.61	60.13
0.50	73.46	70.17	70.44	70.35	70.40	73.72	59.82
0.55	72.82	69.48	69.75	69.66	69.71	73.04	60.00
0.60	72.16	68.75	69.03	68.93	68.98	72.33	59.89
0.65	71.54	68.08	68.36	68.26	68.31	71.67	59.38
0.70	70.96	67.44	67.72	67.62	67.68	71.05	59.51
0.75	70.47	66.91	67.19	67.09	67.14	70.52	57.87
0.80	69.83	66.21	66.50	66.39	66.45	69.84	56.22
0.85	69.09	65.41	65.69	65.59	65.64	69.04	53.24
0.90	68.13	64.37	64.66	64.55	64.61	68.02	50.68
0.95	66.68	62.80	63.09	62.98	63.04	66.47	47.08

Table 3 Values of activation energy (E_a) in kJ mol^{-1} obtained through linear least squares analysis for the isoconversional methods of FWO, KAS, Tang, Starink$^{1.95}$, Starink$^{1.92}$, Bosewell and Friedman for the decomposition reaction

α	E_a/kJ mol^{-1}						
	FWO	KAS	Tang	Starink$^{1.95}$	Starink$^{1.92}$	Bosewell	Friedman
0.10	390.95	400.59	397.89	400.86	400.70	405.93	
0.15	262.61	265.49	263.97	265.76	265.71	270.88	
0.20	220.44	221.07	219.93	221.34	221.32	226.48	
0.25	199.69	199.19	198.29	199.46	199.47	204.64	
0.30	187.17	185.98	185.23	186.25	186.27	191.44	
0.35	179.28	177.64	177.01	177.92	177.94	183.12	112.74
0.40	173.64	171.68	171.12	171.96	171.98	177.18	114.41
0.45	169.62	167.43	166.94	167.70	167.74	172.94	116.57
0.50	166.10	163.69	163.27	163.97	164.01	169.21	115.94
0.55	163.03	160.45	160.06	160.73	160.76	165.98	116.17
0.60	160.24	157.49	157.13	157.77	157.81	163.03	106.47
0.65	157.74	154.84	154.46	155.12	155.16	160.39	103.97
0.70	154.89	151.82	151.43	152.10	152.14	157.38	95.99
0.75	152.01	148.77	148.41	149.05	149.09	154.34	87.01
0.80	148.67	145.24	144.84	145.52	145.57	150.82	73.53
0.85	144.80	141.14	140.72	141.42	141.47	146.74	59.62
0.90	139.78	135.83	135.40	136.12	136.17	141.44	25.90
0.95	132.00	127.61	127.18	127.89	127.96	133.24	289.60

for the two reaction stages, dehydration and thermal decomposition, for the isoconversional methods of KAS, Tang, Starink$^{1.95}$, Starink$^{1.92}$, Bosewell and Friedman are shown in Figs. S1 and S2 (in supporting information). Activation energy obtained for the conversion function $\alpha = 0.05–0.95$ for dehydration and decomposition using different isoconversional methods is given in Tables 2 and 3. Figures 11 and 12 show the E_a versus α curves for dehydration and decomposition reactions for different isoconversional methods. The fluctuations in E_a with α for dehydration and decomposition reactions showed that they follow complex reaction pathways. All E_a versus α curves for each reaction

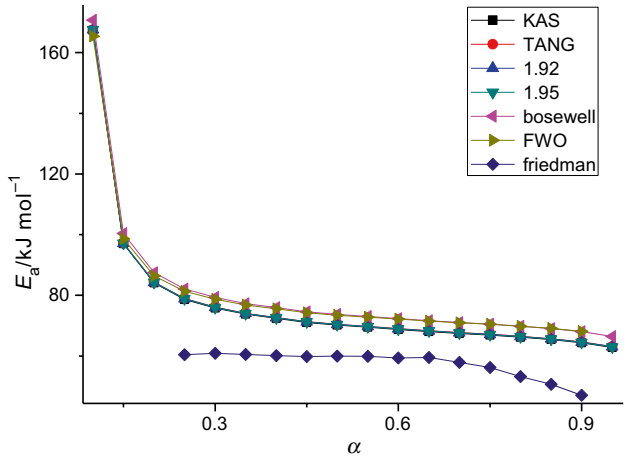

Fig. 11 E_a versus α curves for dehydration reaction for different isoconversional methods FWO, KAS, Tang, Starink$^{1.95}$, Starink$^{1.92}$, Bosewell and Friedman

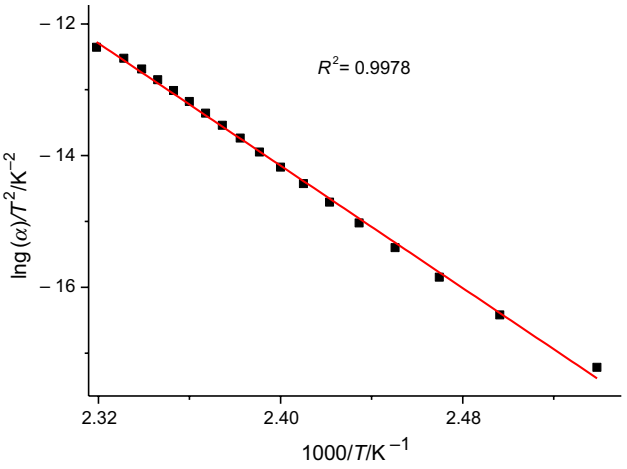

Fig. 13 Model fitting least squares plot (two-dimensional diffusion, D2) for dehydration reaction at a heating rate of 4 K min^{-1}

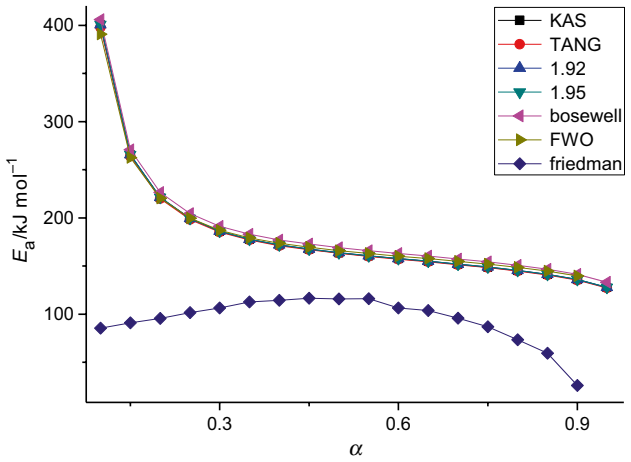

Fig. 12 E_a versus α curves for decomposition reaction for different isoconversional methods FWO, KAS, Tang, Starink$^{1.95}$, Starink$^{1.92}$, Bosewell and Friedman

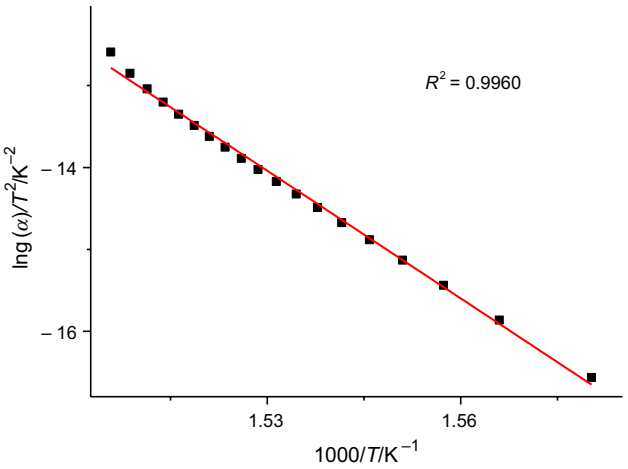

Fig. 14 Model fitting least squares plot (Avrami–Erofeev equation, A2) for decomposition reaction at a heating rate of 4 K min^{-1}

show similar trends of variation of activation energy with α. The dependence of *Ea* on conversion function reveals that the value of *Ea* is independent of α above 40%; however, below 40%, the value is dependent on α. This implies that nucleation and growth in solid require high *Ea*, once the decay commences, i.e., after the completion of nucleation and its growth, decomposition reaction continues with almost constant value of E_a till the end of the process [47].

Model fitting methods were used to suggest the most probable mechanism. For this, the value of ln (g (α)/T^2) versus 1/T of the non-isothermal DSC data at 4 K min^{-1} is plotted. Figures 13 and 14 show model fitting least squares plots for dehydration and decomposition reaction. The plot will be a straight line for a correct mechanism and nonlinear for the inaccurate mechanism. The most probable mechanism for dehydration was found to be with g (α) = (1 − α) * ln(1 − α) + α (i.e., two-dimensional diffusion, D2) and for decomposition g (α) = − ln(1 − α)$^{1/2}$, i.e., Avrami–Erofeev equation A2) whose f(α) = 2 * (1 − α) [− ln(1 − α)]$^{1/2}$.

Frontier molecular orbital analysis

The ability of a molecule to donate or accept electron can be comprehended from the energy of their frontier molecular orbital HOMO and LUMO. The HOMO and LUMO images of zinc oxalate and ZnO are shown in Figs. 15 and 16. HOMO and LUMO energies represent the electron-donating and electron-accepting ability of the molecule,

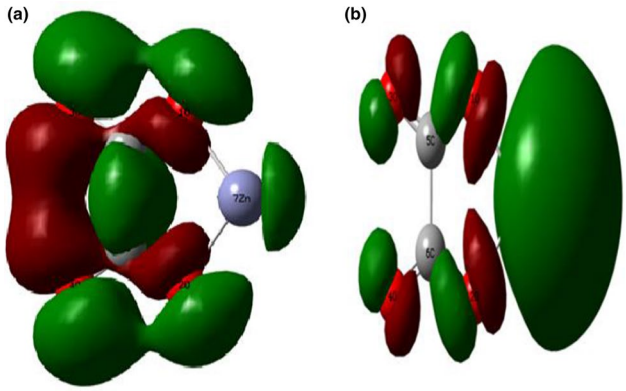

Fig. 15 HOMO (**a**) and LUMO (**b**) of zinc oxalate

respectively. The HOMO, LUMO energies and band gaps of zinc oxalate and ZnO are given in Tables 4 and 5. The band gap obtained for ZnO is 2.54 eV which is comparable with those obtained from the experimental one (3 eV).

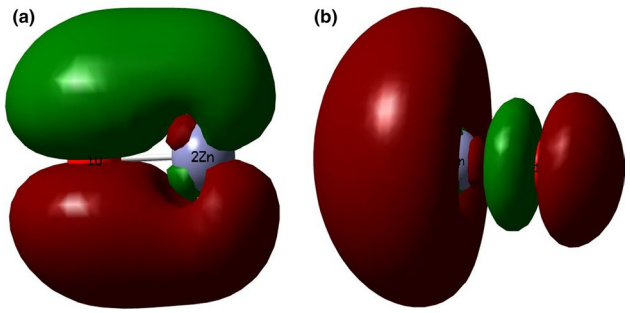

Fig. 16 HOMO (1) and LUMO (2) of ZnO

From the values, it is clear that zinc oxalate has a smaller energy gap than silver oxalate, but larger value than copper oxalate, and hence, its reactivity and stability are between these two [26]. From HOMO and LUMO contours, it is clear that electron density in HOMO is concentrated on carboxylate group, and in LUMO, it is concentrated on Zn. So, in zinc oxalate, there is a possibility of ligand-to-metal charge transfer.

Table 4 HOMO, LUMO energy and the band gap of zinc oxalate

HOMO/eV	LUMO/eV	E_g/eV
− 7.6409	− 5.2273	2.4136

Table 5 HOMO, LUMO energy and the band gap of ZnO

HOMO/eV	LUMO/eV	E_g/eV
− 6.6342	− 4.0953	2.5389

Global reactivity descriptors

The calculated global reactivity descriptors are tabulated in Table 6. The molecule having high HOMO energy shows a better reaction with electrophiles and low LUMO energy prefers reaction with nucleophiles. Since hardness is reflected from the gap between HOMO and LUMO, the hardness of zinc oxalate and hence reactivity are between copper and silver oxalate [26].

The molecular structure of anhydrous zinc oxalate has been optimized through DFT/B3LYP level of theory and 6-31+g (d, p) basis set, and lowest energy structure is confirmed. Frequency calculation was also performed to detect structure having any negative frequency, and the result indicates all frequencies are positive, i.e., there is no imaginary frequency, which confirm the optimized structure is in global minimum. The optimized structure is shown in Fig. 17. The colors blue, red and gray indicate the atom of zinc, oxygen and carbon, respectively. The numbering system of molecule followed GaussView numbering format. The computed bond length values obtained for different bonds in anhydrous zinc oxalate are tabulated in Table 7, and it has been observed that the bond length values decrease in the order Zn–O, C–C, C–O and C=O, and hence, their bond strength increases in the same order. This indicates that the thermal decomposition begins with the breakage of one of the Zn–O bonds leaving a partially anchored zinc oxalate, followed by the breakage of C–C bond with the elimination of CO_2. Finally, C–O bond breaks with the evolution of CO, and ZnO exist as the final decomposition product.

Conclusions

Zinc oxalate dihydrate was synthesized and characterized. The kinetics of dehydration and decomposition were studied by non-isothermal DSC technique in the N_2 atmosphere at four different heating rates. The product of thermal decomposition, ZnO, has been characterized by UV, TEM, SEM-EDAX and XRD and found that the particles are of nanometer range. The

Table 6 Global reactivity descriptors calculated for anhydrous zinc oxalate through orbital vertical method by B3LYP/6-31+g (d, p)

IP/eV	EA/eV	η/eV	χ/eV	S/eV	μ/eV	ω/eV
7.6409	5.2273	1.2068	6.4341	0.4143	− 6.4341	17.1518

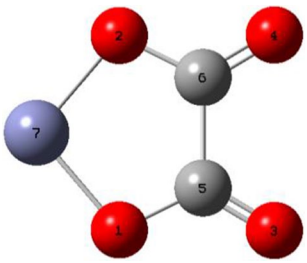

Fig. 17 Optimized structure of zinc oxalate using B3LYP/6-31+g (d, p) as basis set

Table 7 Bond length values obtained for different bonds in anhydrous zinc oxalate through DFT studies using B3LYP/6-31+g (d, p) as basis set

Bond	Bond length/Å
$Zn–O_1$	1.85
$Zn–O_2$	1.85
$C–O_1$	1.36
$C–O_2$	1.36
C–C	1.60
$C=O_1$	1.20
$C=O_2$	1.20

average values of activation energy needed for the different reaction stages are 80.13, 77.22, 77.48, 77.44, 77.39, 80.78, 61.69 (for dehydration reaction), and 183.48, 182.00, 181.29, 182.29, 182.27, 187.51, 109.07 (for decomposition reaction) kJ mol^{-1} obtained using the isoconversional methods of FWO, KAS, Tang, Starink$^{1.92}$, Starink$^{1.95}$ Bosewell and Friedman, respectively. All the isoconversional methods studied show similar trends in the variation of activation energy with the conversion function. Changes in the activation energy with the conversion function for all the isoconversional methods studied reflect complexity of the reaction and changing mechanism during the reaction. Structure and reactivity of zinc oxalate have been investigated using B3LYP/631+g (dp) level of theory using the Gaussian 09W software. From the theoretical investigation and the bond length values, it is concluded that during the thermal decomposition process, first, one of the Zn–O bonds breaks, then C–C bond breaks with the elimination of CO_2, and finally, C–O bond breaks by evolving CO and ZnO that exist as the final decomposition product. Global reactivity descriptors were calculated in order to analyze the extent of reactivity of the molecule.

Acknowledgements The author K. Sabira expresses her sincere gratitude to Human Resource Development Group, Council of Scientific & Industrial Research (CSIR), India, for granting Research Fellowship in the form of CSIR-JRF. The author also acknowledges STIC, CUSAT for TEM analysis and CSIF, University of Calicut, for SEM-EDAX analysis.

References

1. Brown ME, Galwey AK. Thermal decomposition of ionic solids. New York: Elsevier Science; 1999.
2. Mohamed MA, Halawy SA, Salem MA. Non-isothermal decomposition of potassium ferrioxalate trihydrate. J Anal Appl Pyrolysis. 2000;55:55–67.
3. Deb N. An investigation on the solid-state thermal decomposition of bimetallic oxalate and tartrate coordination precursors of lanthanum(III) and palladium(II) ions. J Anal Appl Pyrolysis. 2008;82:223–8.
4. Lvov BV, Boris VL. The physical approach to the interpretation of the kinetics and mechanisms of thermal decomposition of solids: the state of the art. Thermochim Acta. 2001;373:97–124.
5. Boldyrev VV. Thermal decomposition of silver oxalate. Thermochim Acta. 2002;388:63–90.
6. Muraleedharan K, Kripa S. DSC kinetics of the thermal decomposition of copper(II) oxalate by isoconversional and maximum rate (peak) methods. J Therm Anal Calorim. 2014;115:1969–78.
7. Donia AM. Synthesis, identification and thermal analysis of coprecipitates of silver-(cobalt, nickel, copper and zinc) oxalate. Polyhedron. 1997;16:3013–31.
8. Limin G, Hiroyuki A, Norio T. Synthesis of mesoporous metal oxide by the thermal decomposition of oxalate precursor. Langmuir. 2013;29:4404–12.
9. Charu A, Aditi S, Sanju S, Yeshwant N, Gollamudi R. Solid-state reaction of strontium oxalate with uranium oxalate application of TG. J Therm Anal Calorim. 2016;124:43–9.
10. Charu A, Shalu C, Gollamudi R, Yeshwant PN. Application of thermogravimetric analysis in study of solid-state reaction between barium oxalate and uranyl oxalate. J Therm Anal Calorim. 2016;124:51–6.
11. Fatemi NS, Dollimore D, Heal GR. Thermal decomposition of oxalates. Part 16. Thermal decomposition studies on cadmium oxalate. Thermochim Acta. 1982;54:167–80.
12. Gülbanu KC, Halil C, Ramazan D. Thermal and kinetic analysis of uranium salts. Part III. Uranium(IV) oxalate hydrates. J Therm Anal Calorim. 2014;115:2007–20.
13. Ahmad T, Ganguli AK, Ganguly A, Ahmed J, Wani IA, Khatoon S. Chemistry of reverse micelles: a versatile route to the synthesis of nanorods and nanoparticles. Mater Res Soc Symp Proc. 2009;1142:75–88.
14. Kansal SK, Singh M, Sud D. Studies on photodegradation of two commercial dyes in aqueous phase using different photocatalysts. J Hazard Mater. 2007;141:581–90.
15. Zamora PP, Gouvêa CAK, Wypych F, Moraes SG, Durán N, Nagata N. Semiconductor-assisted photocatalytic degradation of reactive dyes in aqueous solution. Chemosphere. 2000;40:433–40.
16. Muruganandham M, Chen IS, Wu JJ. Effect of temperature on the formation of macroporous ZnO bundles and its application in photocatalysis. J Hazard Mater. 2009;172:700–6.
17. Sakthivel S, Neppolian B, Shankar MV, Arabindoo B, Palanichamy M, Murugesan V. Solar photocatalytic degradation of azo dye: comparison of photocatalytic efficiency of ZnO and TiO_2. Sol Energy Mater Sol Cells. 2003;77:65–82.
18. Fujita J, Nakamoto K, Kobayashi M. Infrared spectra of metallic complexes. III. The infrared spectra of metallic oxalates. J Phys Chem. 1957;61:1014–5.
19. Jacob MU, Rerlmutter DD. Thermal decomposition of carbonates, carboxylates, oxalates, acetates, formates, and hydroxides. Thermochim Acta. 1981;49:207–18.
20. Dollimore D. The influence of the environment on the thermal decomposition of oxysalts. J Therm Anal. 1977;11:185–200.

21. Nikumbh AK, Athare AE, Pardeshi SK. Thermal and electrical properties of manganese (II) oxalate dihydrate and cadmium (II) oxalate monohydrate. Thermochim Acta. 1999;326:187–92.
22. Majumdar R, Sarkar P, Ray U, Roy MM. Secondary catalytic reactions during thermal decomposition of oxalates of zinc, nickel and iron(II). Thermochim Acta. 1999;335:43–53.
23. Małecka B, Drozdz-Cieśla E, Małecki A. Mechanism and kinetics of thermal decomposition of zinc oxalate. Thermochim Acta. 2004;423:13–8.
24. Hu C, Mi J, Shang S, Shangguan J. The study of thermal decomposition kinetics of zinc oxide formation from zinc oxalate dihydrate. J Therm Anal Calorim. 2014;115:1119–25.
25. Reshmi S, Vijayalakshmi KP, Thomas D, George BK, Nair CPR. Thermal decomposition of a diazido ester: pyrolysis GC-MS and DFT study. J Anal Appl Pyrolysis. 2013;104:603–8.
26. Sarada K, Vijisha KR, Muraleedharan K. Exploration of the thermal decomposition of oxalates of copper and silver by experimental and computational methods. J Anal Appl Pyrolysis. 2016;120:207–14.
27. Kolezyński A, Małecki A. Theoretical studies of thermal decomposition of anhydrous cadmium and silver oxalates: part II. Correlations between the electronic structure and the ways of thermal decomposition. J Therm Anal Calorim. 2009;96:167–73.
28. Kolezyński A, Małecki A. First principles studies of thermal decomposition of anhydrous zinc oxalate. J Therm Anal Calorim. 2009;96:645–51.
29. Koleżyński A, Małecki A. Theoretical approach to thermal decomposition process of chosen anhydrous oxalates. J Therm Anal Calorim. 2009;97:77–83.
30. Kolezyński A, Małecki A. Theoretical analysis of electronic and structural properties of anhydrous calcium oxalate. J Therm Anal Calorim. 2010;99:947–55.
31. Kolezyński A, Małecki A. Theoretical studies of electronic and crystal structure properties of anhydrous mercury oxalate. J Therm Anal Calorim. 2010;101:499–504.
32. Koleżyński A, Handke B, Drożdż-Cieśla E. Crystal structure, electronic structure, and bonding properties of anhydrous nickel oxalate. J Therm Anal Calorim. 2013;113:319–28.
33. Becke AD. Density-functional thermochemistry. III. The role of exact exchange. J Chem Phys. 1993;98:5648–52.
34. Lee C, Yang W, Parr RG. Development of the Colle–Salvetti correlation-energy formula into a functional of the electron density. Phys Rev B. 1988;37:785–9.
35. Patterson A. The Scherrer formula for X-ray particle size determination. Phys Rev. 1939;56:978.
36. Zhigang J, Daping R, Lixin X, Rongsun Z. Preparation, characterization and photocatalytic activity of porous zinc oxide superstructure. Mater Sci Semicond Process. 2012;15:270–6.
37. Velmurugan R, Swaminathan M. An efficient nanostructured ZnO for dye sensitized degradation of Reactive Red 120 dye under solar light. Sol Energy Mater Sol Cells. 2011;95:942–50.
38. Nelsa A, Alex R, Unni C, Daizy P. Nanostructured ZnO with bio-capping for nanofluid and natural dye based solar cell applications. J Mater Sci Mater Electron. 2017;28:16527–39.
39. Khawam A, Flanagan DR. Role of isoconversional methods in varying activation energies of solid-state kinetics: II. Nonisothermal kinetic studies. Thermochim Acta. 2005;436:101–12.
40. Vyazovkin S. Computational aspects of kinetic analysis. Part C. The ICTAC kinetics projects-data, methods and results. Thermochim Acta. 2000;355:155–63.
41. Starink MJ. The determination of activation energy from linear heating rate experiments: a comparison of the accuracy of isoconversion methods. Thermochim Acta. 2003;404:163–76.
42. Sarada K, Muraleedharan K. Effect of addition of silver on the thermal decomposition kinetics of copper oxalate. J Therm Anal Calorim. 2016;123:643–51.
43. Flynn JH, Wall LA. A quick, direct method for the determination of activation energy from thermo gravi-metric data. Polym Lett. 1966;4:323–8.
44. Ozawa T. A new method of analyzing thermogravimetric data. Bull Chem Soc Jpn. 1965;38:1881–6.
45. Kissinger HE. Reaction kinetics in differential thermal analysis. Anal Chem. 1957;29:1702–6.
46. Wanjun T, Donghua C. New approximate formula for the generalized temperature integral. J Therm Anal Calorim. 2009;98:437–40.
47. Jose John M, Muraleedharan K, Kannan MP, Ganga Devi T. Kinetic studies on the thermal decomposition of phosphate-doped sodium oxalate. J Therm Anal Calorim. 2013;111:137–44.